Doubly Fed Induction Generator System Resonance Active Damping through Stator Virtual Impedance

Song, Yipeng; Wang, Xiongfei; Blaabjerg, Frede

Published in:
I E E E Transactions on Industrial Electronics

DOI (link to publication from Publisher):
10.1109/TIE.2016.2599141

Publication date:
2017

Document Version
Accepted author manuscript, peer reviewed version

Doubly Fed Induction Generator System Resonance Active Damping through Stator Virtual Impedance

Yipeng Song, *Member, IEEE*, Xiongfei Wang, *Member, IEEE*
and Frede Blaabjerg, *Fellow Member, IEEE*

***Abstract*— The penetration of wind power has been increasing in the past few decades all over the world. Under certain non-ideal situations where the wind power generation system is connected to the weak grid, the Doubly Fed Induction Generator (DFIG) based wind power generation system may suffer High Frequency Resonance (HFR) due to the impedance interaction between the DFIG system and the weak grid network whose impedance is comparative large. Thus, it is important to implement an active damping for the HFR in order to ensure a safe and reliable operation of both the DFIG system and the grid connected converters/loads. This paper analyzes and explains first the HFR phenomenon between the DFIG system and a parallel compensated weak network (series RL + shunt C). Then on the basis of the DFIG system impedance modeling, an active damping control strategy is introduced by inserting a virtual impedance (positive capacitor or negative inductor) into the stator branch through stator current feedforward control. The effectiveness of the DFIG system active damping control is verified by a 7.5 kW experimental down-scaled DFIG system, and simulation results of a commercial 2 MW DFIG system is provided as well.**

***Index Terms*— DFIG system impedance, high frequency resonance damping, virtual impedance.**

I. INTRODUCTION

THE renewable power generation has been under continuous development, and the large scale implementation of renewable power generation has been increasing in recent years, with the wind energy and solar energy as the leading technologies [1]-[4]. Many renewable power generation units are connected to the offshore grid or distributed networks, which are small power scale weak networks with comparatively large impedance. As a result, the large number of renewable power generation units may also bring up problems of impedance interaction between the large impedance of weak power network and the impedance of the renewable power generation unit.

Manuscript received January 12, 2016; revised March 15, 2016, May 4, 2016, and June 21, 2016; accepted July 8, 2016.

The authors are all with the Department of Energy Technology, Aalborg University, Aalborg 9220, Denmark (e-mail: yis@et.aau.dk, xwa@et.aau.dk, fbl@et.aau.dk).

For instance, for the radial connection of a typical wind farm configuration where a series compensated capacitor is widely adopted, the Doubly Fed Induction Generator (DFIG) system may suffer Sub-Synchronous Resonance (SSR) [5]-[11] because of the impedance interaction between the DFIG system and the series compensated network. The harmonic linearization method is employed to obtain the positive and negative impedance of the DFIG system in [5]-[7], the influences of PI controller parameters in the rotor current closed-loop control and phase locked loop control are studied concerning the SSR, and the DFIG SSR under different rotor speeds is also investigated. A virtual resistance is inserted to achieve damping of the SSR in [5]. Moreover, the equivalent circuit/impedance modeling of the entire DFIG system and series compensated weak grid network are reported in [8], and the conclusion is that the main reason of the SSR phenomena is the interaction between the electric network and the converter controller. A Thyristor-Controlled Series Capacitor (TCSC) is developed in [9] to flexibly adjust the series compensated capacitance in order to avoid the potential SSR. Furthermore, the SSR is also explained from the perspective of the Nyquist stability criterion in [10]. The design of an auxiliary SSR damping controller and the selection of the control signals in the DFIG converters are explored in [11] in order to effectively mitigate the SSR.

Then, it can be found from the above research that the DFIG system SSR phenomenon has been well analyzed based on the DFIG system impedance modeling results. Therefore when the DFIG is connected to a parallel compensated weak grid, the DFIG system High Frequency Resonance (HFR) may occur and can be similarly analyzed based on the same DFIG system impedance modeling results. The detailed theoretical discussion is conducted in the following parts.

Moreover, for the LCL filter based grid connected converter, the HFR is also likely to interact between the capacitor filter in LCL filter and the equivalent inductor in the weak network. For the purpose of eliminating the HFR, several effective resonance active damping strategies for the grid connected converter have been reported in [12]-[21]. The active damping of the HFR as well as harmonic distortion mitigation in the grid-connected converter is well investigated. The grid current feedback control in [12] is equivalent to adding a virtual impedance across the grid-side inductance,

and it can be represented by a series RL branch in parallel with a negative inductance. The converter with series LC filter, instead of the traditional LCL filter, is studied to achieve the active damping in [13]. A virtual RC impedance is introduced in [15]-[16], i.e., the positive resistance to achieve better damping of harmonic resonance; while the negative inductance to achieve better mitigation of the harmonic distortion by reducing the grid side inductor. For the multi-converter situation, their respective contribution to the harmonic stability of the power system is predicted through the Nyquist diagrams in [17]. The potential oscillations and resonance propagation in the parallel grid-connected converters are mitigated by dynamically reshaping the grid impedance profile seen from the Point of Common Coupling (PCC) [18]. The unknown resonance frequency is first identified by a cascaded adaptive notch filter structure in [19], and then the active damping can be implemented based on the detected resonance frequency. An overview of the virtual impedance based active damping strategy for the grid-connected voltage source and current source converters are summarized in [20], and several alternative methods of implementing the virtual impedance are concluded. Importantly, the interaction coupling between two converters connected to the same PCC or different point of coupling via non-ideal grid is discussed in [21], and also the bifurcation boundaries are derived.

Therefore it can be found that the active damping strategy for the grid connected converter can be modified and adopted to mitigate the HFR in the DFIG system with the implementation of a virtual impedance. The detailed discussion of the DFIG system active damping with virtual impedance will be conducted in following sections.

Thus it is clear that the active damping of HFR requires significant considerations for the DFIG system connected to the parallel compensated weak network. Note that since the series RL weak network and the series compensated weak network (RLC in series) both behave as inductive units in the high frequency range, the HFR is not possible to happen due to the inductive character of the DFIG system, and in this paper the parallel compensated network (series RL + shunt C) is taken into consideration as the weak network configuration. It needs to be pointed out that the shunt (parallel) capacitors are commonly used as static reactive power compensation with the purpose to achieve a high power factor [1]-[3] in the weak network such as micro-grid and standalone network, where the wind power generation system is likely to be applied; besides, the other various renewable power generation units and loads may also behave capacitive seen from PCC. Furthermore, under the circumstances of a cable based weak network, the parasitic capacitance between the transmission cables and grounds [4] is also inevitable, and can vary greatly in practical situation. Thus it is believed that the presence of shunt (parallel) capacitors is reasonable for the discussion topic of this paper. Moreover, the shunt capacitance may vary in a large extent due to several renewable power generation units and various loads which can be connected and disconnected frequently. Thus in certain circumstances, the shunt capacitor in the parallel compensated weak network will unfortunately cause HFR in the DFIG system.

This paper is organized as follows: The impedance modeling of the DFIG machine and Rotor Side Converter (RSC), together with the impedance modeling of Grid Side Converter (GSC) and LCL filter, are established first as foundation for analysis, then the overall DFIG system impedance can be deduced in Section II. The HFR between the DFIG system and the parallel compensated weak network (series RL + shunt C) is analyzed in Section III. The proposed active damping strategy in the DFIG stator branch with the introduction of the positive capacitor or the negative inductor as virtual impedance is illustrated in detail in Section IV. The HFR and the proposed active damping strategy are both validated by simulation results of a 2 MW commercial DFIG system in Section V and experimental results of a 7.5 kW down-scaled DFIG system in Section VI. Finally, the conclusions are given in Section VII.

II. DFIG System Impedance Modeling

The DFIG system impedance modeling has been well established in [5]-[11]. However since the impedance modeling serves as a foundation for the HFR analysis and the proposed active damping strategy, the DFIG system impedance modeling still needs to be described here. Note that, as the LCL filter has better switching harmonics filtering performance than the L filter, the LCL filter [5]-[11] is adopted in this paper. Besides, the mutual inductance, as well as the digital control delay of 1.5 sampling period [7] caused by the voltage/current sampling and the PWM update, are taken into consideration in the impedance modeling.

A. General description of the investigated DFIG system

Fig. 1 shows the configuration diagram of a DFIG system and parallel compensated weak network. As it can be seen, the Rotor Side Converter (RSC) controls the rotor voltage to implement the DFIG machine stator output active and reactive power, the Grid Side Converter (GSC) is responsible for providing a stable dc-link voltage for the RSC, and unlike the previous works [6]-[9] adopting an L filter, the GSC in this paper adopts an LCL filter due to better filtering performance for the switching harmonics, and it is also frequently used in practice.

The three winding transformer is employed to increase the voltage level of both DFIG stator winding and the grid side LCL filter up to a higher voltage level of the PCC. Note that the transformer in the practical applications are always used to change the voltage level, therefore the transformer can be presented as a constant coefficient during the impedance modeling process. For the purpose of explanation simplicity, the transformer is neglected in the DFIG system impedance modeling in the following discussion.

The configuration of parallel compensated network configurations (series RL + shunt C) is adopted as the weak network in the following discussion.

It needs to be pointed out that the impedance modeling in this paper is built in the stationary reference frame, while the

current controllers in the RSC and GSC are both implemented in the synchronous reference frame, therefore the reference frame rotation is as shown in Fig. 1, which will be presented in the impedance modeling results in the following discussions. The control delay caused by the AD sample and PWM update is also inevitable and will be considered too.

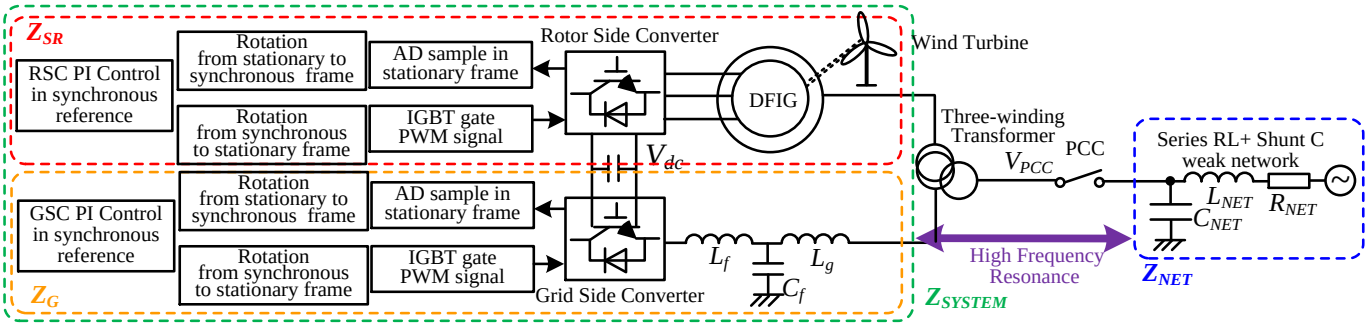

Fig. 1. Configuration diagram of the DFIG system and the parallel compensated weak network, RSC: Rotor Side Converter, GSC: Grid Side Converter

B. GSC and LCL filter impedance modeling

The grid part of the DFIG system contains the GSC and the LCL filter, thus based on [8], the impedance modeling of GSC and LCL filter can be presented as shown in Fig. 2, where $G_c(s\text{-}j\omega_0)$ is the PI current controller containing the proportional part K_{pgsc} and the integral part $K_{igsc}/(s\text{-}j\omega_0)$. The parameters of K_{pgsc} and K_{igsc} can be found in Table I. $G_d(s\text{-}j\omega_0)$ is the digital control delay of 1.5 sampling period. Note that ω_0 is the grid network fundamental component angular speed of 100π rad/s. The introduction of ω_0 is due to the reference frame rotation from stationary frame (where the impedance modeling is built) to the synchronous frame (where the PI closed-loop current control is implemented) as it can be observed from Fig. 1.

Normally, the GSC control has an outer control loop of the dc-link voltage. However, since the dc-link voltage has much longer time constant and slower dynamic response, in this paper the dc-link voltage control loop in the GSC is neglected. The grid synchronization is also neglected in RSC and GSC control for the similar reason of slower dynamic response.

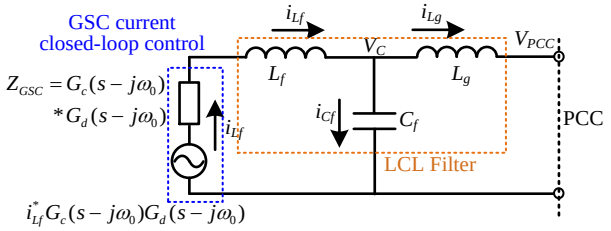

Fig. 2. Impedance modeling of Grid Side Converter (GSC) and LCL filter

Thus, as given in Fig. 2, the GSC current closed-loop control is modeled as one voltage source $i_{Lf}^* G_c(s\text{-}j\omega_0)G_d(s\text{-}j\omega_0)$ in series connection with one impedance $Z_{GSC} = G_c(s\text{-}j\omega_0)G_d(s\text{-}j\omega_0)$.

According to the impedance theory, the impedance of the GSC and LCL filter seen from the PCC can be obtained by setting the voltage source to zero. As a result the impedance of the DFIG grid side (including GSC and LCL filter) Z_G can be deduced as,

$$Z_G = \frac{Z_{Cf}\left(Z_{Lf}+Z_{GSC}\right)+Z_{Lg}\left(Z_{Lf}+Z_{GSC}\right)+Z_{Cf}Z_{Lg}}{Z_{Cf}+\left(Z_{Lf}+Z_{GSC}\right)} \quad (1)$$

where, $Z_{GSC} = G_c(s\text{-}j\omega_0)G_d(s\text{-}j\omega_0)$, $Z_{Cf} = 1/sC_f$, $Z_{Lf} = sL_f$, $Z_{Lg} = sL_g$. L_f, L_g and C_f are the LCL filters.

C. RSC and machine impedance modeling

Based on [8], the impedance modeling of the RSC and DFIG machine can be obtained as shown in Fig. 3.

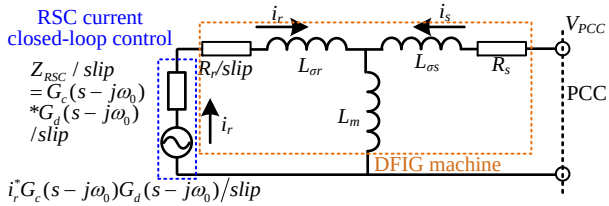

Fig. 3. Impedance modeling of Rotor Side Converter (RSC) and DFIG machine

By setting the rotor control voltage source to zero, the impedance of RSC and DFIG machine seen from the PCC can be obtained as,

$$Z_{SR} = \frac{Z_{Lm}H+\left(R_s+Z_{L\sigma s}\right)H+Z_{Lm}\left(R_s+Z_{L\sigma s}\right)}{Z_{Lm}+H} \quad (2)$$

where $H = (R_r + Z_{RSC})/slip + Z_{L\sigma r}$; $Z_{RSC} = G_c(s\text{-}j\omega_0)G_d(s\text{-}j\omega_0)$; $Z_{Lm} = sL_m$; $Z_{L\sigma r} = sL_{\sigma r}$; $Z_{L\sigma s} = sL_{\sigma s}$. R_s and R_r are stator and rotor resistance, L_m, $L_{\sigma s}$ are $L_{\sigma r}$ the mutual inductance, stator and rotor leakage inductance.

It needs to be noted that the rotor current control and output voltage are both generated in the rotor stationary reference frame and they need to be rotated back to the stationary frame by the slip angular speed expressed as [5]-[7],

$$slip = \left(s - j\omega_r\right)/s \quad (3)$$

where, ω_r is the rotor electric angular speed.

D. DFIG system impedance

As analyzed above, the RSC and DFIG machine, together with the GSC and LCL filter, are connected in parallel to the PCC. Thus the DFIG system impedance is derived based on (1) and (2) as,

$$Z_{SYSTEM} = \frac{Z_G Z_{SR}}{Z_G + Z_{SR}} \quad (4)$$

Bode diagrams of an experimental small scale DFIG system and a commercial (simulated) large scale DFIG system are plotted in Fig. 4(a) and 4(b), with the parameters given in Table I and Table II.

TABLE I
PARAMETERS OF SMALL SCALE DFIG SYSTEM

Rated Power	7500 W	Voltage Level	400 V
L_g	7 mH	L_f	11 mH
C_f	6.6 uF	L_m	79.3 mH
$L_{\sigma s}$	3.44 mH	$L_{\sigma r}$	5.16 mH
R_s	0.44 Ω	R_r	0.64 Ω
K_{prsc}	8	K_{irsc}	16
K_{pgsc}	8	K_{igsc}	16
f_{sw}	5 kHz	T_s	100 μs

TABLE II
PARAMETERS OF LARGE SCALE DFIG SYSTEM

Rated Power	2 MW	Voltage Level	690 V
L_g	125 μH	L_f	125 μH
C_f	220 μF	L_m	3 mH
$L_{\sigma s}$	0.04 mH	$L_{\sigma r}$	0.06 mH
R_s	0.0015 Ω	R_r	0.0016
K_{prsc}	0.2	K_{irsc}	2
K_{pgsc}	0.05	K_{igsc}	2
f_{sw}	2.5 kHz	T_s	200 μs

As it can be observed from Fig. 4(a), for the small scale DFIG system, the Z_{SR} mainly behaves as an inductive unit at the higher frequency range (e.g. above 500 Hz), having a phase response about 90°. For the Z_G, the magnitude response has a peak around 620 Hz and one concave around 966 Hz caused by the LCL filter. The DFIG system impedance Z_{SYSTEM} has similar magnitude and phase response as the Z_G. However, due to the involvement of Z_{SR}, the Z_{SYSTEM} magnitude peak shifts from 620 Hz to 803 Hz, and the phase response within the range of 803 Hz to 966 Hz is also lifted up which is helpful to avoid the HFR (will be explained in the following sections).

On the other hand, the Bode diagram of large scale DFIG system is shown in Fig. 4(b). Since the large scale DFIG system parameters in Table II are much smaller than the small scale DFIG system in Table I, the integral part of PI controller $K_{igsc}/(s\text{-}j\omega_0)$, which can be considered as a virtual capacitance, results in the phase response of Z_G varying between 90° and 270° at the frequency range of 900 Hz to 1400 Hz; while the Z_{SR} remain inductive with phase response of 90° in the entire frequency range. As a result, the DFIG system impedance Z_{SYSTEM} has similar shaping as Z_G, i.e., phase varying from 90° and 270° from 1100 Hz to 1400 Hz, while the phase response is 90° in the frequency range higher than 1400 Hz. This indicates that the interaction between the inductance part of DFIG system and parallel compensated weak network will produce the HFR. The theoretical analysis and simulation results will be given in following.

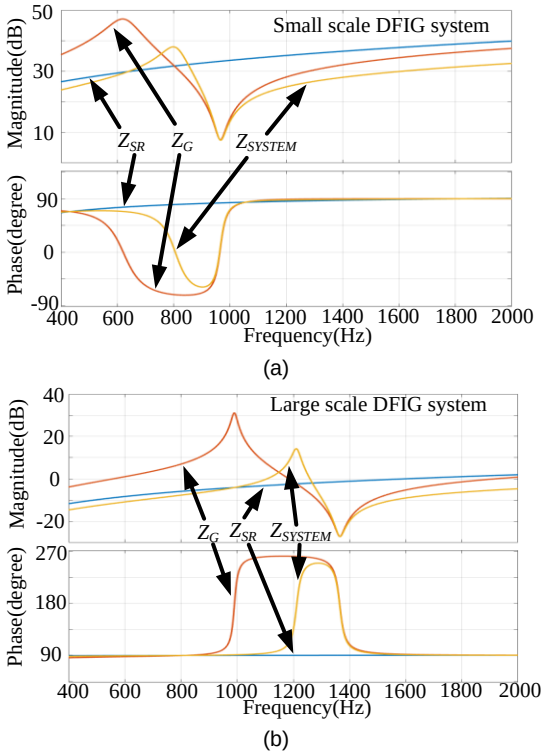

Fig. 4. Bode diagram of (a) the experimental small scale DFIG system (7.5 kW); (b) the simulated large scale DFIG system (2 MW)

III. HFR BETWEEN DFIG SYSTEM AND PARALLEL COMPENSATED NETWORK

As shown in Fig. 4, the DFIG system behaves inductive with the phase response of 90° at high frequency. Thus in order to allow the HFR to happen, the weak network should behave capacitive with the phase response of -90° at the high frequency, then a phase difference of 180° between DFIG system and weak network will be produced, and the HFR occurs consequently. Therefore, the following discussion on the HFR between the DFIG system and weak network will be conducted on the assumption of parallel compensated weak network, i.e., series RL+ shunt C network.

For the case of series RL network which behaves inductive within the entire frequency range, it is impossible to make the HFR to occur. For a series compensated network, i.e., series RLC network in [5]-[11], its phase response at high frequency is identical to the case of series RL network, which will not be described in details here.

The impedance of the series RL and shunt C network can be presented as,

$$Z_{NET\_RL\_C} = \frac{\left(sL_{NET} + R_{NET}\right)/sC_{NET}}{sL_{NET} + R_{NET} + 1/sC_{NET}} \quad (5)$$

where, R_{NET} and L_{NET} are the network series resistor and inductor, C_{NET} is the network shunt capacitor.

Rewriting the impedance of series RL and shunt C network to the following based on (5),

$$Z_{NET\_RL\_C} = \frac{\frac{1}{C_{NET}}s + \frac{R_{NET}}{L_{NET}C_{NET}}}{s^2 + \frac{R_{NET}}{L_{NET}}s + \frac{1}{L_{NET}C_{NET}}} \quad (6)$$

It can be seen from (6) that the peak of the network is determined by L_{NET} and C_{NET}. In this discussion it is assumed that the L_{NET} remains constant, while the C_{NET} will vary and cause the network impedance to shift within a certain frequency range.

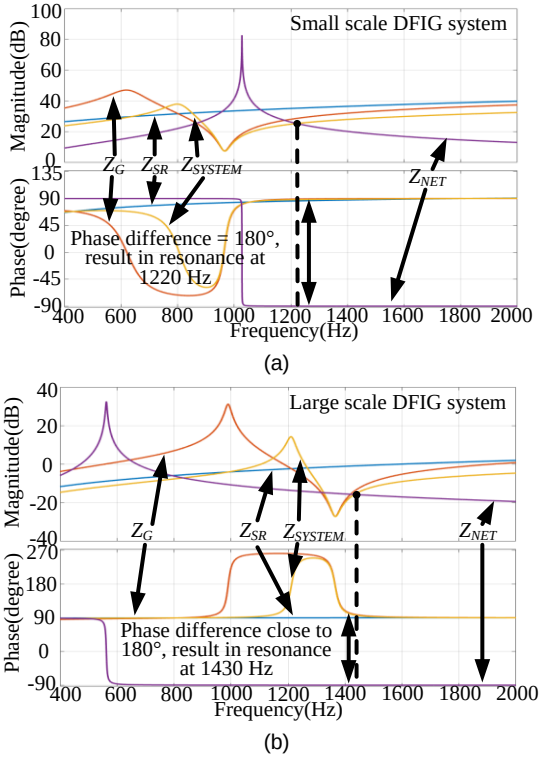

Fig. 5. Bode diagram of (a) the small scale DFIG system impedance in Table I and series RL + shunt C network impedance R_{NET} = 3 mΩ, L_{NET} = 1 mH, C_{NET} = 24 μF; (b) the large scale DFIG system impedance in Table II and series RL + shunt C network R_{NET}= 3 mΩ, L_{NET}= 0.1 mH, C_{NET} = 800 μF

Fig. 5 shows the Bode diagram of both the small scale and large scale DFIG system impedance and series RL + shunt C network impedance. As it is shown in Fig. 5(a), for the case of small scale DFIG in Table I, and the parallel compensated weak network of R_{NET} = 3 mΩ, L_{NET} = 1 mH, C_{NET} = 24 μF, the magnitude intersection point between DFIG system and weak network occurs at 1220 Hz with a phase difference of 180°, thus resulting in the HFR.

Similarly in Fig. 5(b), for the case of large scale DFIG system in Table II, the DFIG system has phase response of 95° at the magnitude intersection frequency of 1430 Hz. This indicates that the DFIG system behaves as positive inductance and negative resistance. While the weak network with parameters R_{NET}= 3 mΩ, L_{NET}= 0.1 mH, C_{NET} = 800 μF in Fig. 5(b) has the phase response of -90°, indicating a negative inductance behavior of the weak network. Therefore, due to the impedance interaction between positive inductance of DFIG system and the negative inductance of weak network, as well as the negative resistance part of the DFIG system which helps to aggravate the resonance, the HFR of 1430 Hz will happen consequently.

It should be pointed out that one magnitude intersection also exists at 820 Hz with a phase difference of 180° in Fig. 4(b). However, due to the lack of negative resistance which exists at the frequency of 1430 Hz, the resonance of 820 Hz is less likely to happen, as proved in the following simulation section.

Thus, it can be found that when connected to the parallel compensated weak network, both the small scale and large scale DFIG system may suffer HFR. The main reason of this resonance is the phase difference of 180° at the magnitude intersection point between the DFIG system and the parallel compensated weak network. It should also be pointed out that the shunt capacitance of 800 μF in Fig. 5(b), which is much larger than that of 24 μF in Fig. 5(a), is reasonable since the small capacitance at the high voltage side of the transmission line will become much larger (square of transformer voltage changing ratio) at the low voltage side of DFIG system due to the existence of voltage level increasing transformer.

IV. Active Damping through Virtual Impedance in Stator Branch

As discussed in the previous section, the HFR will occur as a consequence of impedance interaction between the DFIG system and the parallel compensated weak network.

In order to effectively mitigate the resonance, the impedance of DFIG system needs to be appropriately reshaped, i.e., a virtual impedance [12]-[20] such as the virtual positive capacitor or negative inductor, is employed in the DFIG stator branch in this paper. Due to the limited space available in this paper, the active damping strategy with virtual impedance is illustrated based on the experimental small scale DFIG system. The similar deduction can be conducted for the large scale DFIG system, which is not described here.

A. DFIG system impedance reshaping through virtual impedance in the stator branch

As shown in Fig. 5, the 180° phase difference between the DFIG system and the weak network at the magnitude intersection frequency is the direct reason of the HFR. It is obvious that the HFR can be mitigated if the phase difference at the magnitude intersection point can be reduced, thus a concave in the phase response of the DFIG system is preferred. Since the DFIG system behaves inductive at high frequency, a virtual positive capacitor or negative inductor (whose phase response is -90°) can be introduced to decrease the DFIG system phase response.

Instead of reshaping the DFIG system impedance in the entire frequency range which may interfere with the normal regulation of DFIG output power, a resonant controller with significant capability of frequency selection [15] is employed to reshape the impedance only selectively at the resonance frequency. The Bode diagram of the resonant controller is plotted in Fig. 6, and its expression is given in (7).

$$G_{reso}(s)=\frac{\omega_c s}{s^2+\omega_c s+\omega_{reso}^2} \tag{7}$$

where, ω_{reso} is the resonance frequency, ω_c is the bandwidth parameter.

As it is shown in Fig. 6, its phase response changes across 0°, i.e., from 90° to -90°, and this inherent character of phase response changing 180° around the tuned resonant frequency will result in the opposite behavior of the virtual impedance. For instance, when the positive capacitor and the resonant controller are employed together, the introduced positive capacitor will behave as positive capacitor due to the positive (larger than 0°) phase response of resonant controller within the frequency range lower than the resonant frequency (in green region), while it behaves as a negative capacitor due to the negative (smaller than 0°) phase response of resonant controller within the frequency range higher than the resonant frequency (in red region).

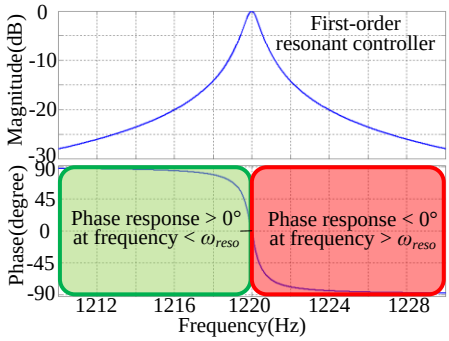

Fig. 6. Bode diagram of the resonant controller in (7)

Based on the above description, it can be concluded that the virtual impedance for the DFIG system HFR damping can be obtained with the resonant controller and virtual impedance units as 1) Positive capacitor + resonant controller; 2) Negative inductor + resonant controller.

According to Fig. 5, the magnitude response of the parallel compensated network Z_{NET} gradually decreases at the potential resonance frequency range higher than 1 kHz, and as a result, it is preferred that the reshaped magnitude of the DFIG system first decreases when lower than the resonance frequency, then increases when higher than the resonance frequency. By reshaping the DFIG system magnitude like this, it can be ensured that only one magnitude intersection point, rather than three points, exists and helps to reduce the possibility of the HFR. The Bode diagram of the reshaped DFIG system impedance is shown in Fig. 8, where the appropriately reshaped DFIG system impedance (in blue) has only one intersection point with the Z_{NET}.

On the other hand, the inappropriate reshaped DFIG system impedance (in red) has three intersection points with the Z_{NET}, which is a failure of the active damping. Further explanation about the appropriate impedance reshaping is given in the description of Fig. 8.

According to Fig. 3 and the positive capacitor / negative inductor + resonant controller virtual impedance, the reshaped impedance modeling can be obtained as shown in Fig. 7. Importantly, since the virtual impedance $Z_{PC/NL}$ is implemented with the stator current feedforward, the digital control delay and PWM update delay of totally 1.5 sample periods also exist when introducing the virtual impedance. Inherently, this control delay is helpful to reduce the phase difference and increase the phase margin.

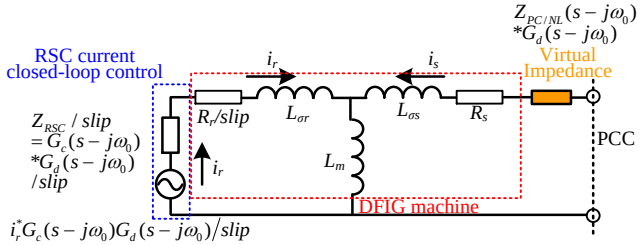

Fig. 7. Impedance modeling of RSC and DFIG machine with the introduction of virtual impedance in the DFIG stator branch through stator current feedforward control

Then the proposed virtual impedance with positive capacitor and resonant controller can be expressed as,

$$Z_{PC}(s)=\frac{\omega_c s}{s^2+\omega_c s+\omega_{reso}^2}\frac{1}{sC_{xrsc}}=\frac{\omega_c/C_{xrsc}}{s^2+\omega_c s+\omega_{reso}^2} \tag{8}$$

where, Z_{PC} is the proposed virtual impedance with positive capacitor, ω_c is the resonant bandwidth parameter, ω_{reso} is the resonant frequency, C_{xrsc} is the proposed virtual positive capacitor.

Thus, based on (8) and Fig. 7, the DFIG system impedance including the virtual positive capacitor in the DFIG stator current feedforward can be presented as,

$$Z_{SYSTEM\_SR\_PC}=\frac{Z_G Z_{SR\_PC}}{Z_G+Z_{SR\_PC}} \tag{9a}$$

$$Z_{SR\_PC}=\frac{Z_{Lm}H+\left(R_s+Z_{L\sigma s}+Z_{PC}G_d\right)H+Z_{Lm}\left(R_s+Z_{L\sigma s}+Z_{PC}G_d\right)}{Z_{Lm}+H} \tag{9b}$$

where, $Z_{SYSTEM\_SR\_PC}$ is the DFIG system impedance with the virtual positive capacitance in the stator branch, Z_{SR_PC} is the DFIG part impedance with the virtual positive capacitance in the stator branch, Z_{PC} is the virtual impedance with positive capacitance, G_d is the digital control delay.

Obviously, the negative inductor has a similar influence on the DFIG system impedance as the positive capacitor, and the combination of negative inductor and resonant controller can be implemented as,

$$Z_{NL}(s)=\frac{\omega_c s}{s^2+\omega_c s+\omega_{reso}^2}*\left(-sL_{xrsc}\right)=\frac{-\omega_c L_{xrsc}s^2}{s^2+\omega_c s+\omega_{reso}^2} \tag{10}$$

where, Z_{NL} is the proposed virtual impedance with negative inductor, $-L_{xrsc}$ is the proposed negative inductor.

Thus, based on (10) and Fig. 7, the DFIG system impedance including the negative inductor virtual impedance in the stator current can be presented as,

$$Z_{SYSTEM\_SR\_NL}=\frac{Z_G Z_{SR\_NL}}{Z_G+Z_{SR\_NL}} \tag{11a}$$

$$Z_{SR\_NL}=\frac{Z_{Lm}H+\left(R_s+Z_{L\sigma s}+Z_{NL}G_d\right)H+Z_{Lm}\left(R_s+Z_{L\sigma s}+Z_{NL}G_d\right)}{Z_{Lm}+H} \tag{11b}$$

where, $Z_{SYSTEM\_SR\_NL}$ is the DFIG system impedance with the virtual negative inductance in the stator branch, Z_{SR_NL} is the DFIG part impedance with the virtual negative inductance in the stator branch.

Note that both (8) and (10) have same denominators, and the numerator of (10) with $s = j\omega_{reso}$ can be written as,

$$-\omega_c L_{xrsc}\left(j\omega_{reso}\right)^2 = \omega_c \omega_{reso}^2 L_{xrsc} \tag{12a}$$

Based on the numerator of (8) and the numerator of (10), if the parameters of L_{xrsc} and C_{xrsc} are chosen according to (12b), then these two kinds of virtual impedances have same inherent character, but just different mathematical expression.

$$\omega_{reso} L_{xrsc} = 1/\left(\omega_{reso} C_{xrsc}\right) \tag{12b}$$

A Bode diagram of DFIG system impedance $Z_{SYSTEM\_SR\_NL}$ with the proposed virtual impedance Z_{SR_NL} of the negative inductor and resonant controller is plotted in Fig. 8, ω_c = 5 rad/s, ω_{reso} = 2π*1220 rad/s, $-L_{xrsc}$ = -150 mH and control delay = 1.5e-4s. Note that the control delay and slip are both taken into consideration in Fig. 8.

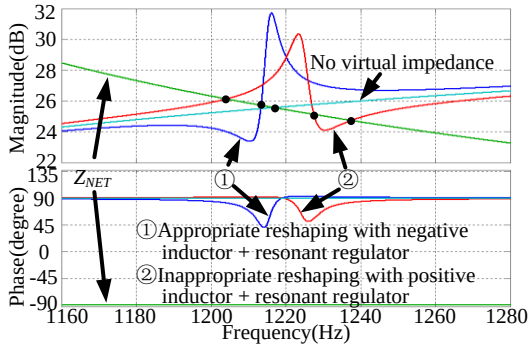

Fig. 8. Bode diagram of the small scale DFIG system impedance considering the proposed virtual impedance Z_{NL} with negative inductor and resonant controller, ω_c = 5 rad/s, ω_{reso} = 2π*1220 rad/s, $-L_{xrsc}$ = -150 mH or C_{xrsc} = 0.11 μF and control delay = 1.5e-4s.

As shown in Fig. 8, when no effective virtual impedance is introduced (in cyan), the DFIG system impedance has a magnitude intersection point with the weak network at around 1220 Hz, and the corresponding phase difference is 180° which results in a HFR at around 1220 Hz.

In contrast, when the virtual impedance with negative inductor is introduced (in blue), the magnitude response of the DFIG system first decreases, then increases, and at last decreases again. This impedance reshaping ensures that only one magnitude intersection at around 1210 Hz exists, and the phase difference at 1210 Hz is effectively reduced to around 132°. Therefore the effective damping of the HFR can be guaranteed.

Nevertheless, if the positive inductor is introduced (in red), the magnitude response of the DFIG system first increases, then decreases, and at last increases again, then there are three magnitude intersections at 1205 Hz, 1227 Hz and 1238 Hz respectively. As it can be seen, the intersection points at 1205 Hz and 1238 Hz still cause resonances.

This inappropriate magnitude reshaping result with positive inductor (in red) in Fig. 8 can be explained as follows:

1) Since the phase response of resonant controller at the frequency range lower than resonant frequency is larger than 0° as shown in Fig. 6, and the proposed positive inductor behaves as positive inductive units, then the magnitude response of the DFIG system impedance will first increase as shown in Fig. 8;

2) On the contrary, since the phase response of resonant controller at the frequency range higher than resonant frequency is lower than 0° as shown in Fig. 6, thus the proposed positive inductor behaves as negative inductive units, thus as a result, the magnitude response of DFIG system impedance will then decrease as shown in Fig. 8.

3) Finally, due to the frequency selection capability of the resonant controller, the proposed positive inductance does not have influence in the frequency range much higher than the resonance frequency, so the DFIG system impedance goes back to the original shape.

4) As a consequence of this inappropriate reshaping with virtual positive inductor, there are three magnitude intersections between DFIG system and weak network, and the active damping fails consequently.

Therefore, based on the above explanations, it can be found that the proposed virtual impedance with the negative inductor + resonant controller is able to appropriately reshape the DFIG system impedance magnitude and phase response. By adjusting the appropriate positive capacitor value to fit (12), C_{xrsc} = 0.11 μF can be yielded, and exactly the same Bode diagram of the DFIG system impedance as shown in Fig. 8 can be obtained and will not be described here.

Thus, it is obvious that the introduced virtual positive capacitor and negative inductor are both capable of appropriately reshaping the DFIG system impedance to mitigate the potential resonance.

B. Parameter design of virtual impedance

In order to achieve successful active damping of the HFR, the parameter of the introduced virtual impedance needs to be carefully designed. According to the numerator of (8) and the numerator of (10), if the parameters of L_{xrsc} and C_{xrsc} are chosen according to (12), then these two kinds of virtual impedance have the same inherent character, but just different mathematical expression. Thus, in the following discussion of the virtual impedance parameter design, the negative inductor under small scale DFIG system is taken as an example.

As shown in Fig. 4(a), the GSC and the LCL filter behave as an inductive unit in the HFR range. Since the impedance of the grid current closed-loop control $Z_{GSC} = G_c(s\text{-}j\omega_0)G_d(s\text{-}j\omega_0)$ is comparatively much smaller than the LCL filter in the resonance frequency range, Z_{GSC} can be neglected, and the impedance of the GSC and LCL filter can be simplified as in the following based on (1),

$$Z_G^{'} = Z_{Lg} + \frac{Z_{Cf} Z_{Lf}}{Z_{Cf} + Z_{Lf}} \tag{13a}$$

By substituting the LCL filter parameters given in Table I into (13a), the impedance of the GSC and LCL filter can be presented as an equivalent inductor L_G as,

$$Z_G^{'} = Z_{Lg} + \frac{Z_{Cf} Z_{Lf}}{Z_{Cf} + Z_{Lf}} \approx sL_G \qquad (13b)$$

Based on (13b) and Table I, the equivalent inductor of GSC and LCL filter at HFR frequency 1220 Hz can be calculated as L_G = 6.8 mH.

For the impedance of RSC and DFIG machine shown in Fig. 5(a), the impedance of the rotor current closed-loop control $Z_{RSC} = G_c(s\text{-}j\omega_0)G_d(s\text{-}j\omega_0)$ is comparatively much smaller in the high frequency range. Also, the stator resistor R_s and rotor resistor R_r can be neglected at the high frequency due to their small value, while the mutual inductor branch can also be neglected since the mutual inductor L_m is much larger than the rotor leakage inductor $L_{\sigma r}$. Therefore, the impedance of the RSC and DFIG machine, with the introduction of virtual impedance, can be simplified as,

$$Z_{SR}^{'} \approx s\left(L_{\sigma s} + L_{\sigma r}\right) - sL_{xrsc}G_d = s\left(L_\sigma - L_{xrsc}G_d\right) \qquad (14)$$

where, $L_\sigma = L_{\sigma s} + L_{\sigma r}$ = 8.6 mH.

Note that the following discussion of parameter design focuses on the specific resonance frequency where the resonant controller has the magnitude response of 0dB and phase response of 0° as proved in (8) and (10), the resonant controller is not included here, but only the virtual negative inductor is included.

Based on (13b) and (14), the DFIG system impedance at the HFR 1220 Hz can be simplified as,

$$Z_{SYSTEM}^{'} \approx \frac{s\left(L_\sigma - L_{xrsc}G_d\right)sL_G}{s\left(L_\sigma + L_G - L_{xrsc}G_d\right)} \qquad (15)$$

It needs to be pointed out that the control time delay G_d of 1.5 sample period can be presented as $G_d(s) = e^{-sT_d}$, thus the introduced negative inductor becomes a combination of the negative inductor $-j\omega_{reso}L_{xrsc}\cos(\omega_{reso}T_d)$ and the negative resistor $-\omega_{reso}L_{xrsc}\sin(\omega_{reso}T_d)$. Note that the negative resistor here is helpful to first decrease and then increase the system magnitude response as shown in Fig. 8. Since the negative resistor does not influence the DFIG system phase response, it can be ignored in the expression of (15), and it can be rewritten as,

$$Z_{SYSTEM}^{'} \approx \frac{\left(L_\sigma - L_{xrsc}\cos(\omega_{reso}T_d)\right)sL_G}{L_\sigma + L_G - L_{xrsc}\cos(\omega_{reso}T_d)} \qquad (16)$$

Obviously, in order to create the phase response concave around the resonance frequency as shown in Fig. 8, a negative sign of (16) with a phase response of -90° is always preferred. As a result, the item $L_\sigma - L_{xrsc}\cos(\omega_{reso}T_d)$ in the numerator and the item $L_\sigma + L_G - L_{xrsc}\cos(\omega_{reso}T_d)$ in the denominator are preferred to have opposite sign. Note that in this paper, the resonance frequency f_{reso} = 1220 Hz as discussed above, and the control time delay T_d = 1.5e-4 s, thus $\cos(\omega_{reso}T_d)$ = 0.4.

1) When $L_{xrsc}\cos(\omega_{reso}T_d) < L_\sigma$

Under this circumstance, both the $L_\sigma - L_{xrsc}\cos(\omega_{reso}T_d)$ in the numerator and the $L_\sigma + L_G - L_{xrsc}\cos(\omega_{reso}T_d)$ in the denominator have positive sign, so (16) has a positive sign, which means that the phase response concave of the DFIG system impedance can not be created, and instead, the phase response between the Z_{SYSTEM} and Z_{NET} becomes larger than 180° with a negative inductor of -15 mH as shown in Fig. 9. This results in a failure of the HFR damping.

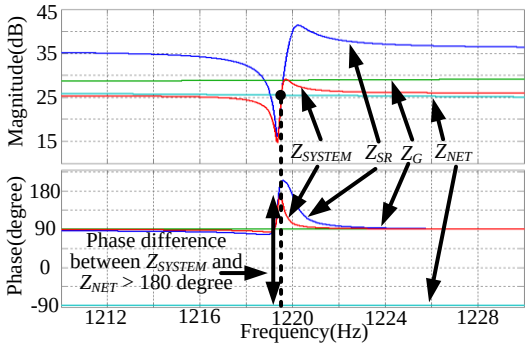

Fig. 9. Bode diagram of the DFIG system impedance considering the proposed virtual impedance Z_{NL}, ω_c = 5 rad/s, ω_{reso} = 2π*1220 rad/s, -L_{xrsc} = -15 mH or C_{xrsc} = 1.1 μF, control delay = 1.5e-4s.

2) When $L_\sigma < L_{xrsc}\cos(\omega_{reso}T_d) < L_\sigma + L_G$

Under this circumstance, the $L_\sigma + L_G - L_{xrsc}\cos(\omega_{reso}T_d)$ in the denominator remains always a positive sign. The item $L_\sigma - L_{xrsc}\cos(\omega_{reso}T_d)$ in the numerator has a negative sign at the exact resonance frequency point, but unfortunately it has a positive sign around the resonance frequency point due to the dramatic magnitude dropping around the resonant frequency shown in Fig. 6. This means that the DFIG system can behave as capacitive at the exact resonance frequency, while remains inductive around the resonance frequency.

Most important, in this case, the HFR may occur between Z_{SR} and Z_G (inside the DFIG system) with a virtual negative inductor of -30 mH, as shown in Fig. 10. It can be seen that the phase difference between Z_{SYSTEM} and Z_{NET} can be successfully reduced to 60°. Unfortunately at the same time, the phase difference between Z_{SR} and Z_G is 180°, thus causing the parallel resonance of Z_{SR} and Z_G within the DFIG system interior as a consequence. Again, this case also fails to mitigate the HFR.

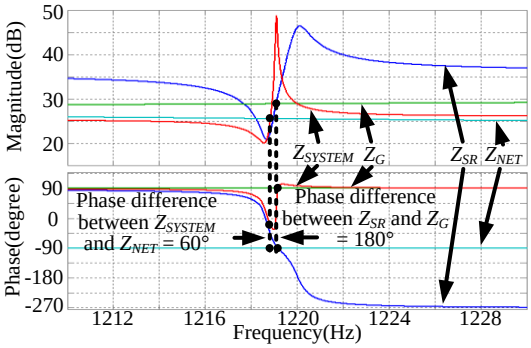

Fig. 10. Bode diagram of the DFIG system impedance considering the proposed virtual impedance Z_{NL}, ω_c = 5 rad/s, ω_{reso} = 2π*1220 rad/s, -L_{xrsc} = -30 mH or C_{xrsc} = 0.55 μF, control delay = 1.5e-4s.

3) When $L_\sigma + L_G < L_{xrsc}\cos(\omega_{reso}T_d)$

In this case, the item $L_\sigma - L_{xrsc}\cos(\omega_{reso}T_d)$ in the numerator has a negative sign all around the resonance frequency point. The item $L_\sigma + L_G - L_{xrsc}\cos(\omega_{reso}T_d)$ in the denominator has a negative sign at the exact resonance frequency, but due to the dramatic magnitude dropping around the resonant frequency shown in Fig. 6, the item

$L_\sigma + L_G - L_{xrsc}\cos(\omega_{reso}T_d)$ would have a positive sign around the resonance frequency. This situation indicates that the DFIG system impedance has a phase concave in the frequency range lower than the resonance frequency, which can be seen from Fig. 11. As a result, the phase difference between Z_{SYSTEM} and Z_{NET} can be reduced to 120°, ensuring a successful mitigation of HFR. Besides, the phase difference between Z_{SR} and Z_G is 135°, indicating no resonance inside the DFIG system.

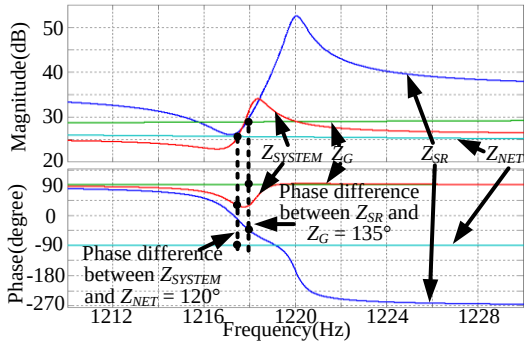

Fig. 11. Bode diagram of the DFIG system impedance considering the proposed virtual impedance Z_{NL}, ω_c = 5 rad/s, ω_{reso} = 2π*1220 rad/s, -L_{xrsc} = -60 mH or C_{xrsc} = 0.275 μF, control delay = 1.5e-4s.

Thus, it can be concluded that, based on above analysis on the virtual impedance design, the virtual negative inductor (or positive capacitor) needs to be large (or small) enough, as shown in (17), to create the DFIG system impedance phase response concave and simultaneously avoid the resonance within DFIG interior Z_{SR} and Z_G, and thus finally to achieve a successful resonance damping.

$$L_{xrsc} > \frac{L_\sigma + L_G}{\cos(\omega_{reso}T_d)} \tag{17a}$$

$$C_{xrsc} < \frac{\cos(\omega_{reso}T_d)}{\omega_{reso}^2\left(L_\sigma + L_G\right)} \tag{17b}$$

C. block diagram

Fig. 12 shows the control block diagram of the HFR active damping strategy implemented in RSC. As it can be seen, for the RSC control, an enhanced phase locked loop (PLL) is able to provide the information of grid voltage fundamental synchronous angular speed ω_1 and angle θ_1 information, while an encoder gives out the DFIG rotor position θ_r and speed ω_r. The rotor current $\boldsymbol{I}^+_{rdq}$ is first sampled and then regulated based on the reference value $\boldsymbol{I}^{+*}_{rdq}$ with PI controller to output the harvested wind energy to the power grid. The stator current $\boldsymbol{I}^+_{sdq}$ is also sampled for the feedforward control with the introduction of virtual impedance. The block '2r/3s' indicates the reference frame rotation from three phase stationary frame to two phase synchronous frame.

The resonance frequency detection unit [19], which employs an Adaptive Notch Filter (ANF) structure based on the multiple ANFs and Frequency-Locked Loops (FLLs), is adopted to detect and output the resonance frequency ω_{reso}, so that the proposed virtual impedance with positive capacitor or negative inductor can be flexibly adjusted based on various resonance frequencies. On the basis of the detected resonance frequency, the stator current together with the proposed virtual positive capacitor or negative inductor can be used to achieve the active damping of the HFR.

The output of the rotor current PI closed-loop control $\boldsymbol{V}^+_{rdqPI}$ and the output of active damping $\boldsymbol{V}^+_{sdqPC\_NL}$, are added, together with the decoupling compensation, giving out the rotor control voltage $\boldsymbol{V}^+_{rdq}$, which is then transformed to the rotor stationary frame and delivered as the input to the Space Vector Pulse Width Modulation (SVPWM).

As for the GSC control, the dc-link voltage V_{dc} is well regulated by a PI controller, and its output is delivered as converter side inductance filter current reference $\boldsymbol{I}^{+*}_{fdq}$, which is used to regulate the actual converter side inductance filter current $\boldsymbol{I}^+_{fdq}$ by a PI controller. Similarly, the GSC control voltage $\boldsymbol{V}^+_{gdq}$ can be obtained by the PI current controller output and the decoupling compensation unit.

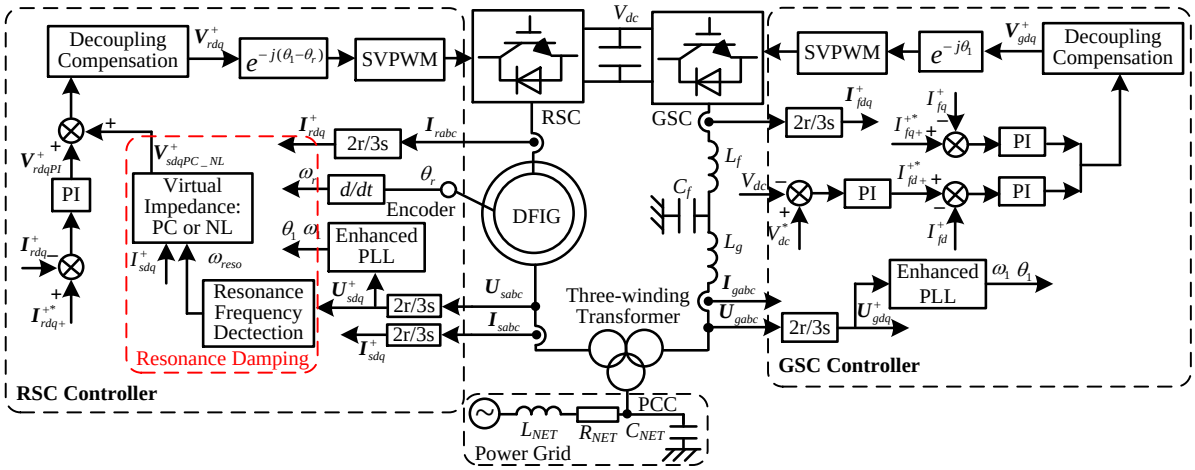

Fig. 12. Control block diagram of the DFIG system HFR active damping strategy through a stator virtual impedance, i.e., Positive Capacitance (PC) or Negative Inductance (NL)

V. Simulation Validation

A. Simulation setup

In order to validate the HFR phenomenon in the large scale commercial 2 MW DFIG system, a simulation model based on MATLAB/Simulink is built up, its parameters are given in Table II.

The weak network parameters are chosen as the same in the theoretical analysis section, i.e., R_{NET} = 3 mΩ, L_{NET} = 0.1 mH, C_{NET} = 800 μF. It should be pointed out that the large shunt network capacitance is possible, since the small capacitance at the high voltage side of the transmission line will become much larger (square of transformer voltage changing ratio) at the low voltage side of DFIG system due to the existence of voltage level increasing transformer. The sampling and switching frequency of both RSC and GSC are 5 kHz and 2.5 kHz respectively. The dc-link voltage is set to 1200 V. Stator output active and reactive power is respectively 1.0 p.u. and 0.0 p.u., the rotor speed is 0.8 p.u.

B. Simulation results

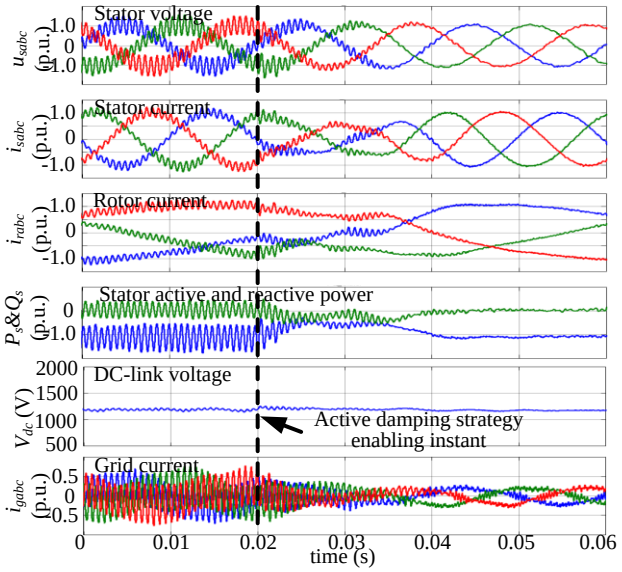

Fig. 13. Simulation result of 2 MW large scale DFIG system when shunt capacitance C_{NET} = 800 μF, R_{NET} = 3 mΩ, L_{NET} = 0.1 mH in the weak grid network when the active damping strategy is enabled (a) system response; (b) FFT analysis result of stator voltage after active damping.

Fig. 13 gives out the simulation results of DFIG system when the active damping strategy is enabled. Before the active damping strategy is enabled, the HFR occurs in the entire DFIG system; once enabled, the active damping strategy is able to mitigate the HFR within around 20 ms, and the sinusoidal stator current, rotor current and grid current, as well as smooth stator output active and reactive power and dc-link voltage can be achieved. It can be analyzed that the stator voltage contains the HFR of 63.4% 1475 Hz (which is close to the theoretical analysis result of 1430 Hz in Fig. 5(b)); then, the stator voltage resonance component can be successfully suppressed to 0.14% 1475 Hz. Therefore, the effectiveness of the proposed active damping strategy can be verified in the large scale commercial DFIG system.

VI. Experimental Validation

A. Experimental setup

In order to experimentally validate the correctness of the proposed active damping strategy in the small scale DFIG system HFR through the stator current feedforward, a down-scaled 7.5 kW experimental test rig is built up as shown in Fig. 14.

The experimental DFIG system parameters can be found in Table I. The weak network is simulated using a three phase inductor and capacitor. The DFIG is externally driven by a prime motor, and two 5.5 kW Danfoss motor drives are used for the GSC and the RSC, both of which are controlled with dSPACE 1006. The rotor speed is set 1200 rpm (0.8 p.u.), with the synchronous speed of 1500 rpm (1.0 p.u.). The dc-link voltage is 650 V. The switching frequency f_{sw} for both RSC and GSC is 5 kHz, the sample frequency f_s for both RSC and GSC is 10 kHz. The voltage level of the DFIG system is 400 V. During the experiment, a transformer is connected between DFIG stator winding and the PCC to prevent grid connection inrush current and the circulating current, the rated voltage of transformer is 400 V, and the turn ratios between primary side and secondary side is 1:1, which means this transformer does not change the voltage level between primary and secondary winding. The experimental validation is conducted under the weak network parameters of R_{NET} = 3 mΩ, L_{NET} = 1.5 mH, C_{NET} =10 μF.

B. Experimental results

Fig. 15 shows the experimental result of the DFIG system when active damping control strategy is disabled under sub-synchronous speed of 1200 rpm (0.8 p.u.). As a consequence of the impedance interaction between the DFIG system and the parallel compensated weak network grid, a HFR around 1600 Hz occurs in three phase stator voltage and current, rotor current, grid side voltage and current.

It should be noted that during the experimental validation process, the prime motor is driven by a general converter which will inject high frequency switching noise to the power grid and as a consequence the u_g in all the experimental results Fig. 15 - Fig. 17 contain switching noise due to the weak power grid impedance. This switching noise can be filtered out by the transformer leakage inductance, thus the stator voltage u_s in all the experimental results do not contain the noise. Considering that this noise does not influence the resonance active damping performance and the experimental results can still be used to validate the active damping method.

The dynamic response of the DFIG system at the instant of enabling the active damping strategy is shown in Fig. 16. As it can be observed, the HFR components in all the stator voltage and current, as well as the grid side voltage and current can effectively be mitigated within 10 ms once the damping is enabled, which guarantees a good dynamic performance in a practical application.

Besides the experimental results under sub-synchronous speed, the cases under super-synchronous speed are also experimentally validated with the results shown in Fig. 17. Fig. 17 similarly provides the dynamic response of the DFIG system when the active damping strategy is enabled at super-synchronous speed of 1700 rpm (1.13 p.u.). The fast dynamic response time of around 10 ms can also be achieved, which is beneficial to the damping of the HFR.

Therefore, the experimental results are able to validate the effectiveness of the proposed active damping control strategy for the DFIG system HFR from the perspective of both steady state response and fast dynamic response.

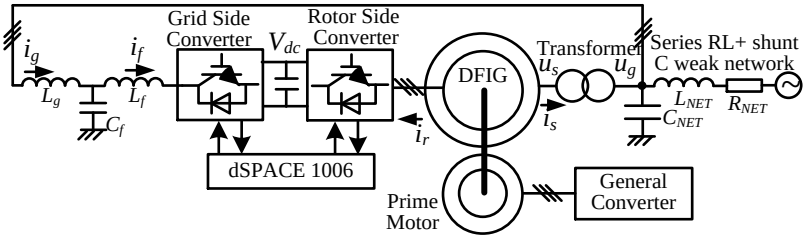

Fig. 14. Setup of 7.5 kW DFIG system test rig

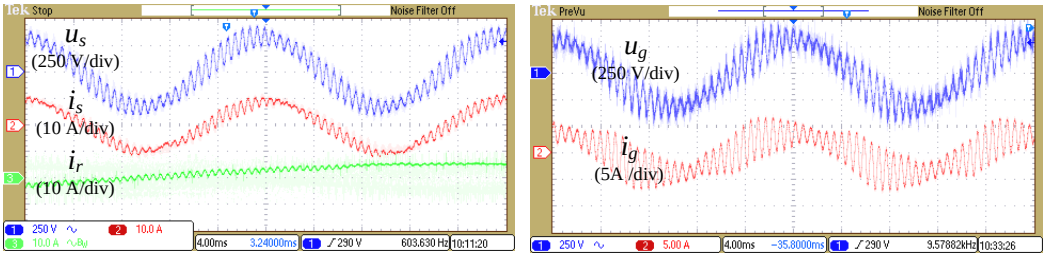

Fig. 15. Steady state response of DFIG system with active damping strategy disabled at sub-synchronous speed of 1200 rpm (0.8 p.u.), weak network parameters of R_{NET} = 3 mΩ, L_{NET} = 1.5 mH, C_{NET} =10 μF

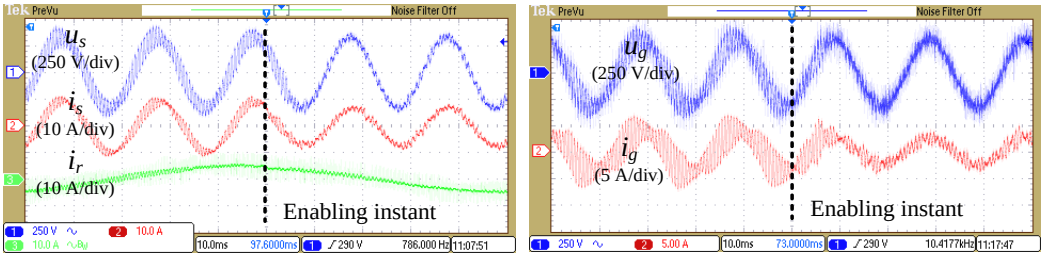

Fig. 16. Dynamic response of DFIG system when active damping strategy is enabled, at sub-synchronous speed of 1200 rpm (0.8 p.u.), weak network parameters of R_{NET} = 3 mΩ, L_{NET} = 1.5 mH, C_{NET} =10 μF

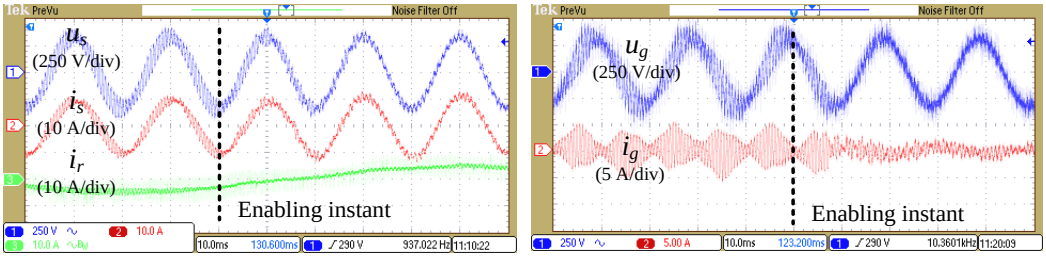

Fig. 17. Dynamic response of DFIG system when active damping strategy is enabled, at super-synchronous speed of 1700 rpm (1.13 p.u.), weak network parameters of R_{NET} = 3 mΩ, L_{NET} = 1.5 mH, C_{NET} =10 μF

VII. Conclusion

This paper has investigated the HFR phenomenon and the corresponding active damping control strategy for DFIG system under parallel compensated weak network with the implementation of virtual impedance in the DFIG stator current feedforward control.

1) The HFR can be analyzed and explained based on the impedance modeling of the DFIG system and the parallel compensated weak network.
2) The stator current feedforward in the RSC is implemented with the introduction of a virtual positive capacitor or a virtual negative inductor to achieve the active damping performance by appropriately reshaping the DFIG system magnitude and phase response.
3) The simulation results and experimental results verify the correctness of the HFR theoretical analysis results and also the effectiveness of the proposed active damping strategy in terms of both steady state response and fast dynamic response under both sub- and super-synchronous DFIG rotor speed.

References

[1] F. Blaabjerg, and K. Ma, "Future on Power Electronics for Wind Turbine Systems," *IEEE J. Emer. Sel. Topics Power Electron.*, vol. 1, no. 3, pp. 139-152, Sep. 2013.

[2] V. Yaramasu, B. Wu, P. C. Sen, S. Kouro, and M. Narimani, "High-power wind energy conversion systems: State-of-the-art and emerging technologies," *Proceedings of the IEEE*, vol. 103, no. 5, pp. 740 – 788, 2015.
[3] Z. Chen, J. M. Guerrero, and F. Blaabjerg, "A Review of the State of the Art of Power Electronics for Wind Turbines," *IEEE Trans. on Power Electron*., vol. 24, no. 8, pp. 1859 – 1875, 2009.
[4] X. Wang, F. Blaabjerg, and P. C. Loh, "Proportional derivative based stabilizing control of paralleled grid converters with cables in renewable power plants," *in Proc. Energy Conversion Congress and Exposition* (ECCE), pp. 4917 - 4924, 2014.
[5] I. Vieto, and J. Sun, "Damping of Sub-synchronous Resonance Involving Type-III Wind Turbines," *in Proc. Control and Modeling for Power Electronics* (COMPEL), pp. 1-8, 2015.
[6] I. Vieto, and J. Sun, "Small-Signal Impedance Modeling of Type-III Wind Turbine," *in Proc. Power & Energy Society General Meeting* (PESG), pp. 1-5, 2015.
[7] I. Vieto, and J. Sun, "Real-time Simulation of Sub-synchronous Resonance in Type-III Wind Turbines," *in Proc. Control and Modeling for Power Electronics* (COMPEL), pp. 1-8, 2014
[8] Z. Miao, "Impedance-Model-Based SSR Analysis for Type 3 Wind Generator and Series-Compensated Network," *IEEE Trans. Energy Convers.*, vol. 27, no. 4, pp. 984–991, Dec. 2012.
[9] L. Piyasinghe, Z. Miao, J. Khazaei, and L. Fan, "Impedance Model-Based SSR Analysis for TCSC Compensated Type-3 Wind Energy Delivery Systems," *IEEE Trans. Sustainable Energy.*, vol. 6, no. 1, pp. 179–187, Jan. 2015.
[10] L. Fan, and Z. Miao, "Nyquist-Stability-Criterion-Based SSR Explanation for Type-3 Wind Generators," *IEEE Trans. Energy Convers.*, vol. 27, no. 3, pp. 807–809, Sep. 2012.
[11] L. Fan, and Z. Miao, "Mitigating SSR Using DFIG-Based Wind Generation," *IEEE Trans. Sustainable Energy.*, vol. 3, no. 3, pp. 349–358, July 2012.
[12] X. Wang, F. Blaabjerg, and P. C. Loh, "Grid-Current-Feedback Active Damping for LCL Resonance in Grid-Connected Voltage Source Converters," *IEEE Trans. Power Electron*., vol. 31, no. 1, pp. 213-223, Jan. 2016.
[13] X. Wang, Y. Pang, P. C. Loh, and F. Blaabjerg, "A Series-LC-Filtered Active Damper With Grid Disturbance Rejection for AC Power-Electronics-Based Power Systems," *IEEE Trans. Power Electron*., vol. 30, no. 8, pp. 4037-4041, Aug. 2015.
[14] X. Wang, F. Blaabjerg, and P. C. Loh, "Virtual RC Damping of LCL-Filtered Voltage Source Converters With Extended Selective Harmonic Compensation," *IEEE Trans. Power Electron*., vol. 30, no. 9, pp. 4726-4737, Sep. 2015.
[15] X. Wang, F. Blaabjerg, and Z. Chen, "Synthesis of Variable Harmonic Impedance in Inverter-Interfaced Distributed Generation Unit for Harmonic Damping Throughout a Distribution Network," *IEEE Trans. Ind. Appl*., vol. 48, no. 4, pp. 1407-1417, July-Aug. 2012.
[16] X. Wang, F. Blaabjerg, and Z. Chen, "Autonomous Control of Inverter Interfaced Distributed Generation Units for Harmonic Current Filtering and Resonance Damping in An Islanded Microgrid," *IEEE Trans. Ind. Appl*., vol. 50, no. 1, pp. 452-461, Jan.-Feb. 2014.
[17] X. Wang, F. Blaabjerg, and W. Wu, "Modeling and Analysis of Harmonic Stability in an AC Power-Electronics-Based Power System," *IEEE Trans. Power Electron*., vol. 29, no. 12, pp. 6421-6432, Dec. 2014.
[18] X. Wang, F. Blaabjerg, M. Liserre, Z. Chen, J. He, and Y. Li, "An Active Damper for Stabilizing Power-Electronics-Based AC Systems," *IEEE Trans. Power Electron*., vol. 29, no. 7, pp. 3318-3329, July 2014.
[19] X. Wang, F. Blaabjerg, and M. Liserre, "An Active Damper to Suppress Multiple Resonances with Unknown Frequencies," *in Proc. Applied Power Electronics Conference and Exposition* (APEC), pp. 2184-2194, 2014.
[20] X. Wang, Y. Li, F. Blaabjerg, and P. C. Loh, "Virtual-Impedance-Based Control for Voltage-Source and Current-Source Converters," *IEEE Trans. Power Electron*., vol. 30, no. 12, pp. 7019-7037, Dec. 2015.
[21] C. Wan, M. Huang, C. K. Tse, and X. Ruan, "Effects of Interaction of Power Converters Coupled via Power Grid: A Design-Oriented Study," *IEEE Trans. Power Electron*., vol. 30, no. 7, pp. 3589-3600, July 2015.
[22] J. Hu, H. Nian, H. Xu, and Y. He, "Dynamic Modeling and Improved Control of DFIG under Distorted Grid Voltage Conditions," *IEEE Trans. Energy Convers.*, vol. 26, no. 1, pp. 163-175, March 2011.

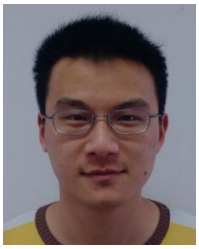

Yipeng Song (S'14-M'16) was born in Hangzhou, China. He received the B.Sc. degree and Ph.D. degree both from the College of Electrical Engineering, Zhejiang University, Hangzhou, China, in 2010 and 2015. He is currently working as a Postdoc at the Department of Energy Technology in Aalborg University, Denmark. His current research interests are motor control with power electronics devices in renewable-energy conversion, particularly the control and operation of doubly fed induction generators for wind power generation.

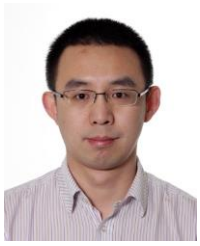

Xiongfei Wang (S'10-M'13) received the B.S. degree from Yanshan University, Qinhuangdao, China, in 2006, the M.S. degree from Harbin Institute of Technology, Harbin, China, in 2008, both in electrical engineering, and the Ph.D. degree from Aalborg University, Aalborg, Denmark, in 2013. Since 2009, he has been with the Aalborg University, Aalborg, Denmark, where he is currently an Assistant Professor in the Department of Energy Technology. His research interests include modeling and control of grid-connected converters, harmonics analysis and control, passive and active filters, stability of power electronic based power systems.

He received an IEEE Power Electronics Transactions Prize Paper award in 2014. He serves as the Associate Editor of IEEE TRANSACTIONS ON INDUSTRY APPLICATIONS and the Guest Associate Editor of IEEE JOURNAL OF EMERGING AND SELECTED TOPICS IN POWER ELECTRONICS Special Issue on Distributed Generation.

Frede Blaabjerg (S'86–M'88–SM'97–F'03) was with ABB-Scandia, Randers, Denmark, from 1987 to 1988. From 1988 to 1992, he was a Ph.D. Student with Aalborg University, Aalborg, Denmark. He became an Assistant Professor in 1992, Associate Professor in 1996, and Full Professor of power electronics and drives in 1998. His current research interests include power electronics and its applications such as in wind turbines, PV systems, reliability, harmonics and adjustable speed drives.

He has received 17 IEEE Prize Paper Awards, the IEEE PELS Distinguished Service Award in 2009, the EPE-PEMC Council Award in 2010, the IEEE William E. Newell Power Electronics Award 2014 and the Villum Kann Rasmussen Research Award 2014. He was an Editor-in-Chief of the IEEE TRANSACTIONS ON POWER ELECTRONICS from 2006 to 2012. He is nominated in 2014 and 2015 by Thomson Reuters to be between the most 250 cited researchers in Engineering in the world.